Icarus 226 (2013) 1128–1137

Contents lists available at ScienceDirect

Icarus

journal homepage: www.elsevier.com/locate/icarus

The temperature and width of an active fissure on Enceladus measured with *Cassini* VIMS during the 14 April 2012 South Pole flyover

Jay D. Goguen [a,*], Bonnie J. Buratti [a], Robert H. Brown [b], Roger N. Clark [c], Phillip D. Nicholson [d], Matthew M. Hedman [d], Robert R. Howell [a,e,1], Christophe Sotin [a], Dale P. Cruikshank [f], Kevin H. Baines [a], Kenneth J. Lawrence [a], John R. Spencer [g], David G. Blackburn [h]

[a] *Jet Propulsion Laboratory, 4800 Oak Grove Drive, Pasadena, CA 91109, United States*
[b] *University of Arizona, Lunar and Planetary Laboratory, Tucson, AZ 85721, United States*
[c] *US Geological Survey, Denver, CO 80225, United States*
[d] *Astronomy Dept., Cornell University, Ithaca, NY 14853, United States*
[e] *University of Wyoming, Dept. of Geology and Geophysics, Laramie, WY 82071, United States*
[f] *NASA Ames Research Center, Moffett Field, CA 94035, United States*
[g] *Southwest Research Institute, Boulder, CO 80302, United States*
[h] *The Planetary Institute for Space Research and Technologies, Lowell, AR 72745, United States*

ARTICLE INFO

Article history:
Received 30 March 2013
Revised 5 July 2013
Accepted 8 July 2013
Available online 24 July 2013

Keywords:
Enceladus
Infrared observations
Geological processes
Satellites, Surfaces
Saturn, Satellites

ABSTRACT

The width and temperature of the active fissures on Saturn's satellite Enceladus provide key observable constraints on physical models of these geyser-like eruptions. We analyze a sequence of high spatial resolution near-infrared spectra acquired with VIMS at 0.025 s intervals during a 74 km altitude flyover of the South Pole of Enceladus by the Cassini spacecraft on 14 April 2012 UTC. A thermal-emission spectrum covering 3- to 5-μm wavelengths was detected as the field of view crossed one of the four major fissures, Baghdad Sulcus, within 1 km of 82.36S latitude and 28.24W longitude. We interpret this spectrum as thermal emission from a linear fissure with temperature 197 ± 20 K and width 9 m. At the above wavelengths, the spectrum is dominated by the warmest temperature component. Looking downward into the fissure at only 13° from the vertical, we conclude that our results measure the temperature of the interior fissure walls (and the H_2O vapor) at depths within 40 m of the surface.

1. Introduction

One of the most exciting discoveries from the NASA/ESA Cassini spacecraft orbiting Saturn is the unexpected activity from the South Pole region of Enceladus, a small 250-km-radius inner icy Moon (Dougherty et al., 2006). Four prominent fissures, dubbed the tiger stripes, are the source of active plumes: high-velocity jets comprised mostly of H_2O molecules and ice grains, some of which escape the satellite's gravity and populate Saturn's faint E-ring (Hansen et al., 2006; Porco et al., 2006; Postberg et al., 2009; Ingersoll and Ewald, 2011). The Composite Infrared Spectrometer (CIRS) measured strong thermal emission from Enceladus' South Pole region with the warmest emission concentrated along these linear fissures (Spencer et al., 2006). The mechanism for the subsurface heating is poorly understood and a topic of intense interest (Hurford et al., 2007; Spencer et al., 2009). Although there may be a liquid water reservoir beneath the South Pole with the H_2O-dominated plume generated by exposure of the liquid to the vacuum of space through cracks (Matson et al., 2012; Postberg et al., 2011), alternative hypotheses that do not require H_2O liquid have been proposed (Kieffer et al., 2006, 2009). The high spatial resolution near-infrared measurements reported here provide important new constraints on such models of the physics of the heat transfer to the surface.

The Visual Infrared Mapping Spectrometer (VIMS) covers the critical 3–5 μm wavelength range that includes the short wavelength rising edge of the Planck blackbody emission spectrum for the relevant ~200 K fissure temperatures and measures the warmest temperature component of the emission. In this regard, VIMS provides an ideal complement to the spectra from Cassini's CIRS instrument which covers wavelengths from 6.7 to several hundred μm, where extended areas that include cooler temperatures also contribute significantly to the emission spectrum.

* Corresponding author. Address: Mail Stop 183-401, Jet Propulsion Laboratory, 4800 Oak Grove Drive, Pasadena, CA 91109, United States.
E-mail address: Jay.D.Goguen@jpl.nasa.gov (J.D. Goguen).
[1] On sabbatical at the Jet Propulsion Laboratory during part of this work.

0019-1035/$ - see front matter © 2013 Elsevier Inc. All rights reserved.
http://dx.doi.org/10.1016/j.icarus.2013.07.012

2. Enceladus plume fly-through on 14 April 2012 UTC

VIMS observed one of the fissures, Baghdad Sulcus, at exceptionally high resolution during a spectacularly low 74-km-altitude pass by the Cassini spacecraft over Enceladus' South Pole at a velocity of 7.5 km s^{-1}. The trajectory was designed to enable *in situ* sampling of the plume composition with the Ion and Neutral Mass Spectrometer (INMS) and Cosmic Dust Analyzer (CDA). The orientation of the spacecraft was chosen to point the VIMS and CIRS instruments towards Enceladus' surface so that their fields of view were 'dragged' across the fissure region at the spacecraft velocity in a ride-along mode with no independent control of their pointing. At this speed, the entire diameter of Enceladus was traversed in 67 s. During this observation, much of Enceladus' South Pole region was not illuminated by the Sun providing optimum conditions for detecting endogenic thermal emission against an otherwise cold and dark background.

VIMS spectra were acquired in the 'occultation mode' designed for rapid sampling of the signal from a star as it is occulted by Saturn's rings or Titan's atmosphere (Brown et al., 2004). VIMS acquired a continuous series of 0.025-s integration time spectra covering the 3- to 5-μm wavelength range for a single hi-resolution pixel (0.25 × 0.50 mrad, scan mirror stationary). The pixel footprint on Enceladus' surface is 38 m in the across-track direction and 214 m in the along-track direction parallel to the spacecraft velocity. The along-track footprint length is determined mainly by the 7.5 km s^{-1}spacecraft velocity during the integration.

3. Results

A 25.6 s section within the series of spectra acquired as the spacecraft traversed the South Pole region at closest approach is shown in Fig. 1. We detected a bright source of thermal emission contained within a single integration when the field of view crossed Baghdad Sulcus, one of the four major fissures. There is no comparable emission detected in any of the other 1023 spectra obtained during this interval. It is noteworthy that there is no measurable thermal emission in either the spectrum acquired just 0.025 s before or 0.025 s after the detection. The adjacent-sample non-detections are only separated by 214 m from the detection location and set an upper limit on the size of the emission source and the temperature gradient. The CIRS instrument simultaneously detected a strong thermal source (Spencer et al., 2012).

3.1. Location

The surface track of the VIMS field of view across Enceladus' South Pole region is shown in Fig. 2. To provide context for the VIMS measurements, the locations of the spectra are plotted over the best image (18 m/pixel) of this region acquired in November 2009 by the Imaging Science Subsystem (ISS) when the South Pole was still illuminated by sunlight. The location of the thermal source on the background image is uncertain by ±1 km due to the combination of uncertainties in the precise shape and orientation of Enceladus, spacecraft position, local topography, and instrument pointing at the two epochs of the background image and the VIMS measurement. It is likely that the actual thermal source lies on the linear Baghdad Sulcus fissure at its closest point to the location shown in Fig. 2C and Table 1.

The remainder of this section provides some detailed supporting information on determination of the latitude and longitude of the source of the thermal emission and its location relative to the Imaging Sub-System (ISS) Narrow Angle Camera image (NASA Planetary Data System image N1637462854_1) in Fig. 2. The coordinates (Table 1) are planetocentric latitude and West longitude

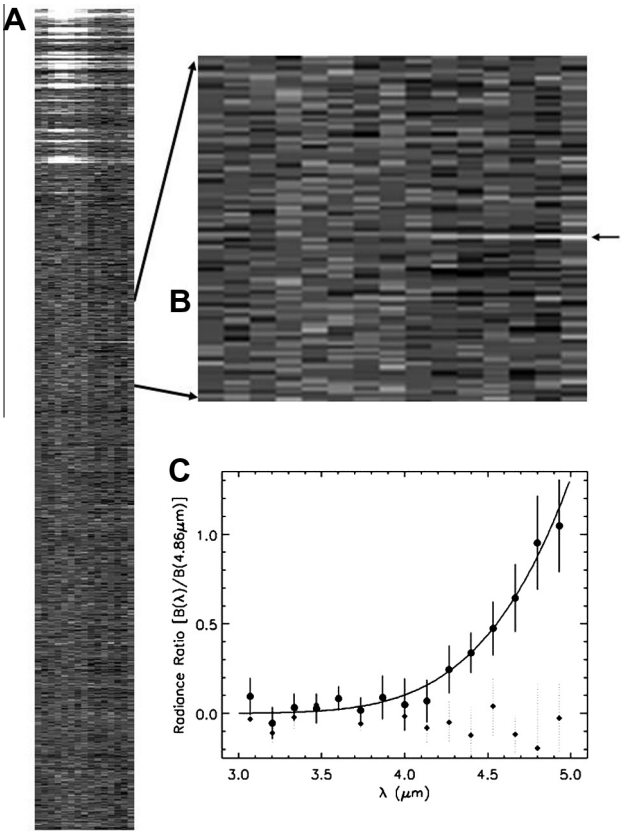

Fig. 1. (A) 1024 spectra, acquired during 25.6 s as Cassini passed over Enceladus' nighttime South Pole, shown as an image with each image line displaying a single 0.025 s integration. Time increases from bottom to top and wavelength increases from 3.0 μm at left to 5.0 μm at right. Strong signals at top are reflected sunlight after terminator crossing. (B) Magnified section of A showing the thermal emission spectrum that is apparent in only a single integration indicated by the arrow. (C) The wavelength variation of the emission identified by the arrow in B and normalized at 4.86 μm (circles) compared to the average of the preceding and following integrations (diamonds) when VIMS measured no emission. The solid line shows the spectrum for the best fit color temperature of 197 ± 20 K. The area sampled during an integration is 214 by 38 m.

Table 1
Summary of results.[a]

Latitude	Longitude	Error	Temperature	Error	Width[b]
82.36S	28.24W	±1 km	197 K	±20 K	9 m

[a] Cassini VIMS measurements acquired during sequence S73, Parameter Set ID VIMS_164EN_ENCEL18001, start times 2012-105T14:01:54.762Z and 2012-105T14:00:02.671Z.

[b] Fill factor 12%; for a discussion of the limits on widths and temperatures, see Section 4.1 and Table 2.

on the tri-axial ellipsoid with $(a,b,c) = (256.6, 251.4, 248.3)$ km (Thomas et al., 2007) and the IAU 2009 updated prime meridian (Archinal et al., 2010). The NAIF toolkit software package (Acton, 1996) with the reconstructed Cassini kernels was used to determine the coordinates of each VIMS sample. As a check on the absolute pointing, the time when the field of view crossed the bright limb of Enceladus was calculated and compared to the observed time of the bright limb crossing which occurred 0.050 s after the calculated time. The coordinates in Table 1 include this small correction (~375 m along track) to match the measured limb crossing time.

To overlay the calculated VIMS sample positions on the ISS image, we used the USGS ISIS version 3 software (Anderson et al., 2004), which uses the same NAIF geometry routines and data

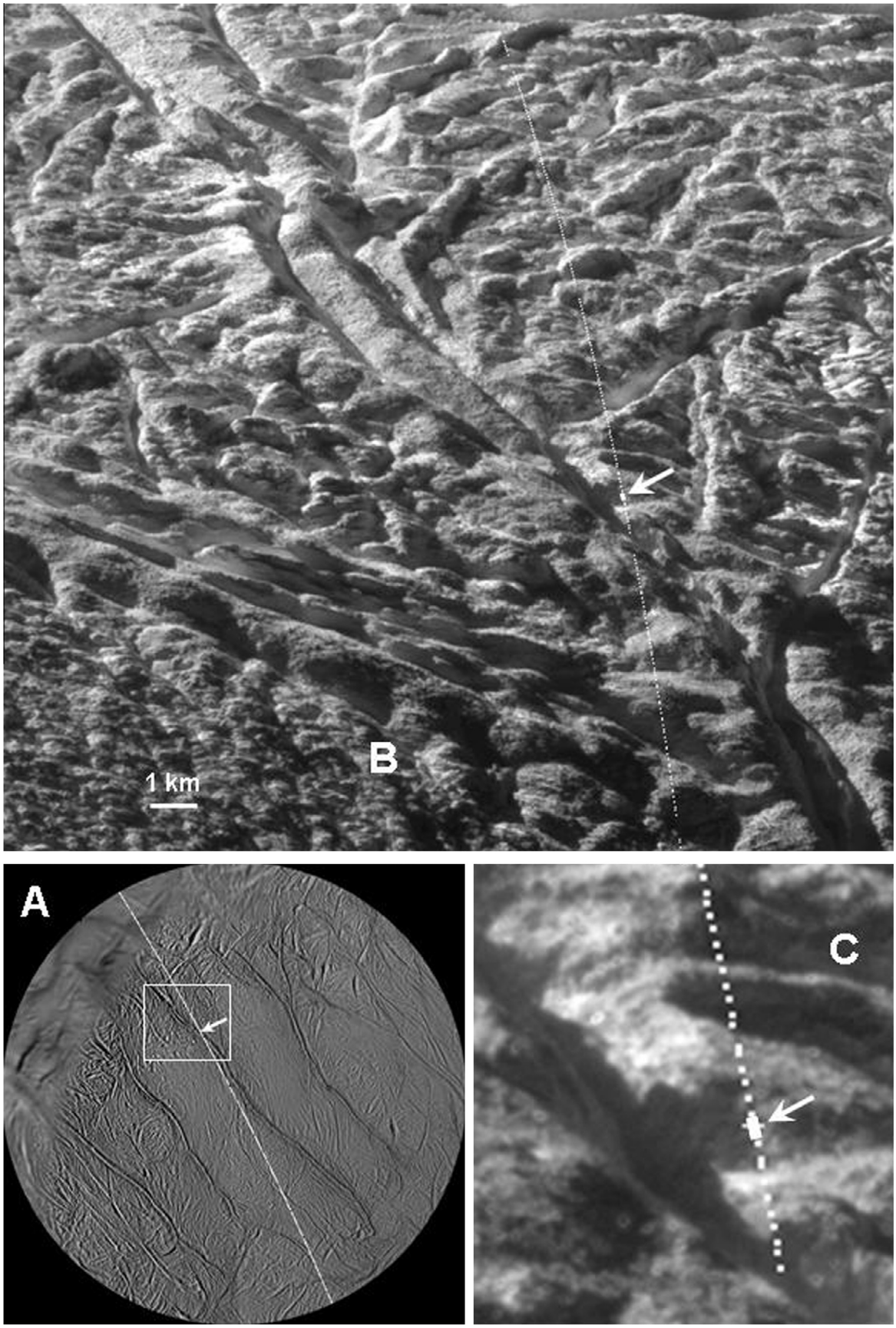

Fig. 2. (A) Dots show the location of each spectrum plotted on a Cassini controlled mosaic of Enceladus' South Pole (Roatsch et al., 2008). The position of the spectrum shown in Fig. 1C is indicated by the arrow where the trajectory crosses Baghdad Sulcus. (B) The best Cassini image (PDS N1637462854_1) acquired in daylight in November 2009 of the region in the box in A with a 1 km scale bar at the lower left. (C) Portion of B showing the size and location (white rectangle indicated by arrow) of the pixel footprint that contains the hot source. The location uncertainty is consistent with the source lying within the nearby fissure.

files, to get the coordinates of each image pixel on the same ellipsoid model (Thomas et al., 2007; Archinal et al., 2010). The South Pole region of Enceladus for latitudes south of 65°S is depressed relative to the ellipsoid by an average of 344 m as indicated in Fig. 5a of Thomas et al. (2007). Because the ISS image views the surface from a steep angle of 66° from the vertical, this 344 m depression of the region imaged results in a shift of 42.5 pixels along the azimuth of the spacecraft. With this shift of the image, both the ISS image display and the VIMS sample coordinates are registered with the tri-axial ellipsoid shape model. This approach of directly comparing the location data from the independent VIMS and ISS observations has the advantage of avoiding introduction of a third intermediate controlled mosaic for which there is no satisfactory way to register the VIMS non-image data. The disadvantage is that there is no independent check on the navigation of either data set, except for the VIMS sunlit limb measurement already described. The uncertainty in the location is estimated to be ±1 km.

4. Discussion

4.1. Interpretation of spectra

For a blackbody at a uniform temperature, the wavelength dependence of the radiance depends only on the temperature. The "color" temperature that best fits the normalized spectrum in Fig. 1C is 197 ± 20 K. To match the absolute radiance measured, the Planck radiance spectrum must be weighted by a multiplicative 'fill factor', defined as the ratio of the measured signal to the signal that would be measured if the same temperature source completely filled the pixel during the entire integration. During one integration time, this definition accounts for the time an emitting sub-pixel area spends in the instrument field of view as it sweeps over a region 10 times longer than the instantaneous 19-m along-track dimension of the pixel. A fill factor of only 12% is required to match the radiance spectrum for the best fit color temperature (Fig. 3). This indicates that the emitting source area is small compared to the area sampled during the integration which is illustrated by the small white rectangle in Fig. 2C.

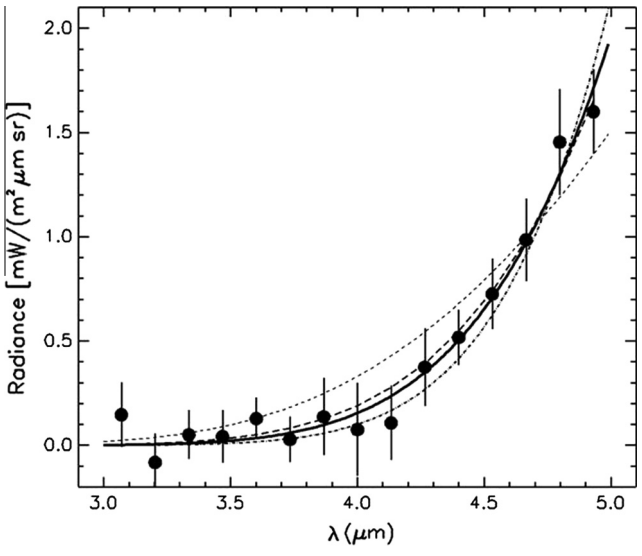

Fig. 3. Absolute radiance spectrum (circles with error bars) compared to a range of isothermal fissure models (lines). Solid line is the best fit 197 K color temperature and a fill factor of 12% (Table 2, case a). Dash-dot line is the lower limit temperature 172 K and a fill factor of 100% (Table 2, case b). Dashed line is ice at its melting temperature 273 K and a fill factor of 0.15% (Table 2, case c). The long-dashed line is a non-isothermal model, a 'zero-width' fissure where all of the radiance is contributed by conduction heating of the ice in contact with a vertical plane held at a constant $T = 236.5$ K (Table 2, case f).

Qualitatively, we expect that emission from the warm interior walls of the fissure will dominate the VIMS spectrum because the 3–5 μm wavelengths sample the rising edge of the Planck radiance function for ~200 K temperatures relevant to these fissures. These wavelengths are most sensitive to the highest temperature present. This thermal emission is clearly closely associated with the long linear fissure of Baghdad Sulcus and linear models for the geometry of the emitting area are used in most previous studies (Schmidt et al., 2008; Abramov and Spencer, 2009; Spencer et al., 2010). Assuming a linear isothermal fissure model, the width of the fissure determines the absolute radiance level, but has no effect on the wavelength dependence of the spectrum. A simple approximate relationship between the fill factor, f, and the width, w, of the fissure is $w = fvt \tan\theta$, where v is the ground velocity of the VIMS pixel, t is the integration time and θ is the 24° angle between the along track direction and the fissure azimuth at the point where they intersect. This "square wave" approximation for w is compared to the exact calculation in Appendix A and is accurate to <10% for the VIMS observation geometry. For the best fit 197 K color-temperature model, the width of the fissure corresponding to $f = 0.12$ is 9 m. This temperature is 20 K warmer than the highest reported Enceladus temperature from CIRS 7–9 μm spectra, 177 ± 1 K (Spencer et al., 2010). The relationship between temperature and fissure width is discussed in greater detail in Section 4.1.2.

4.1.1. Constraints on the temperature gradient from the non-detections in the adjacent sample spectra

The non-detections of emission in the two adjacent spectra bracketing the measured emission (Fig. 1) provide a new observational constraint on the temperature gradient perpendicular to the fissure. Our measured upper limit for the integrated radiance over the 3–5 μm wavelength range for the average of the two adjacent spectra is <7% of the wavelength-integrated radiance for the spectra that includes the detection. Abramov and Spencer (2009) model the thermal profile perpendicular to the fissure that results from conduction of heat through the ice and warming the adjoining surface which we will call the "margins". We interpolate their model results to estimate the temperature and thermal emission due to heat conducted through the ice walls of the fissure to test whether thermal emission should have been detected in the two adjacent samples. The 3–5 μm integrated radiance in the adjacent samples from the conductively heated fissure margins for a 197 K fissure is only 3×10^{-5} of that from the detection sample, well below our 7% measured upper limit. As shown in Fig. 3 of Abramov and Spencer (2009), the temperature decreases approximately proportional to log (distance), dropping 47 K from 1 to 10 m for their 225 K model and 30 K for their 175 K model. For the adjacent sample radiance to exceed our upper limit, the temperature would have to decrease much more slowly with distance from the fissure at a rate of less than 23 K over the distance from 1 to 10 m. We conclude that our non-detections in adjacent samples are consistent with the expected temperature distribution due to conduction of heat through the fissure walls.

Although additional heating of the adjoining margins terrain may result from condensation of the fraction of vapor that does not escape and from fallback of warm solids that are ejected at low velocity, it is difficult to estimate the resulting temperature distribution. The solids to vapor ratio in the plumes is poorly constrained (Ingersoll and Ewald, 2011; Hedman et al., 2009), as is the fraction of the vapor that condenses near the vent. Future models for this component, or any other hypothesized heating, will be constrained by our measured lower limit on the temperature gradient

orthogonal to the fissure derived from the non-detections in the adjacent samples.

4.1.2. What area dominates the VIMS thermal emission spectrum?

A related question that is important to the interpretation of our spectrum is: what fraction of the signal within the detection sample originates from the conductively heated fissure margins, that is, are we measuring the temperature of the warmest ice visible between the fissure walls, or does most of the radiance VIMS detects come from the cooler but larger fissure margins area?

Lacking measurements of the active fissure width, some previous studies have assumed narrow fissures significantly warmer than 200 K. Abramov and Spencer (2009) successfully model 9–16 μm CIRS spectra of 6-km scale areas with a zero-width, constant $T \sim 225$ K fissure that conducts heat to warm the adjacent terrain. Finite fissure widths were considered and also fit the data, but the width could not be tightly constrained. Ingersoll and Pankine (2010) model the transport of heat by hydrodynamic flow of warm water vapor escaping through model fissures for a range of fissure geometries and widths up to 1 m. For their models 1–4, the temperature at the top of the fissure varies from 211 to 227 K, with higher temperatures corresponding to narrower widths. Narrower and warmer fissures can also reproduce our spectrum and we discuss these models in detail Sections 4.1.2.1 and 4.1.2.2.

4.1.2.1. Isothermal models. Fig. 3 shows our best fit absolute radiance spectrum for T_{color} = 197 K and a fissure width of 9 m. Two limiting cases are also shown. The lower limit temperature case assumes the VIMS field of view was completely filled (100% fill factor) during the duration of the integration, an improbable situation where the fissure happens to exactly match the size of the field of view. Wider and cooler fissures than this limiting case are ruled out by the non-detections in adjacent integrations. The upper limit temperature case assumes all of the emission is radiated at the melting temperature of ice and corresponds to a fissure width of only 11 cm. We include this T_{melt} case only to illustrate that the spectrum puts a tight upper limit on the area of melting temperature ice that could be present in the sample. If liquid water supplies the vapor within the fissure, the reservoir likely exists at km depths (Schmidt et al., 2008; Ingersoll and Pankine, 2010), much deeper than the few tens of m sampled in our spectrum. Neither of these extreme cases fit the measured spectra as well as the T_{color} model.

The simple temperature, fill factor fits to the radiance spectrum assume that the emission from the sampled area comes from an isothermal source. These isothermal fits have the advantage that they are a straightforward parameterization of the spectrum, but they are limited because they do not include relevant physics that can produce other temperature distributions that fit the spectrum equally well. Two published studies examine some relevant physics and provide a context within which we consider our spectrum. Abramov and Spencer (2009) model conduction of heat through the ice walls of the fissure and Ingersoll and Pankine (2010) model hydrodynamic gas flow through a fissure.

4.1.2.2. Non-isothermal models. Within the fissure, heat exchange between the warm water vapor and the fissure walls determines the temperature of the walls (Ingersoll and Pankine, 2010). At the top of the fissure, the ice surface just outside the fissure walls will be heated by conduction due the strong temperature gradient between the warm walls and the 75 K background temperature of Enceladus surface (Abramov and Spencer, 2009; Ingersoll and Pankine, 2010). For narrow fissure models at higher temperatures, this conductive heating of the fissure margins will raise the surface temperature, and consequently the radiance in the VIMS wavelength range, so that the VIMS spectrum could be dominated by radiation from the fissure margins rather than from the fissure itself. Abramov and Spencer (2009) model the temperature as a function of the distance from a constant temperature wall due to heat conducted through the ice for the boundary condition of cooling by radiation at the surface. To quantify the effects of including the conductively heated margins (surface adjacent to but outside the fissure walls), in analyzing our spectrum, we interpolate the results from (Abramov and Spencer (2009), their Fig. 3) to add the contribution of the conductively heated margins to the radiance spectrum for fissure models defined by the fissure temperature and width.

What combinations of fissure width and temperature are allowed by fits to the VIMS spectrum? Fig. 4 shows the relationship between fissure width and temperature for the suite of these conduction-included models that give the best fit to the VIMS spectrum. The solid curve in Fig. 4 was determined by holding the width constant and finding the best fit temperature for each width. When the radiance contribution from the margins is included in the model and both the width and temperature are free parameters, the best fit to the VIMS spectrum is T = 200.9 K and width = 5.5 m (Fig. 4, + symbol), about 4 K warmer and 40% narrower than the simple T_{color} isothermal model. The radiance spectra for these two cases are indistinguishable if both were plotted in Fig. 3.

The T_{color} isothermal fit assumes that all of the VIMS detected radiance comes from the fissure. An alternative to this fissure-dominated model is the margins-dominated end member model corresponding to a zero-width fissure where all of the radiance is contributed by the margins heated by conduction from a vertical plane held at a constant temperature (Abramov and Spencer, 2009). To fit the VIMS spectrum, the temperature of this zero-width fissure is 236.5 K and the spectrum is plotted as the long-

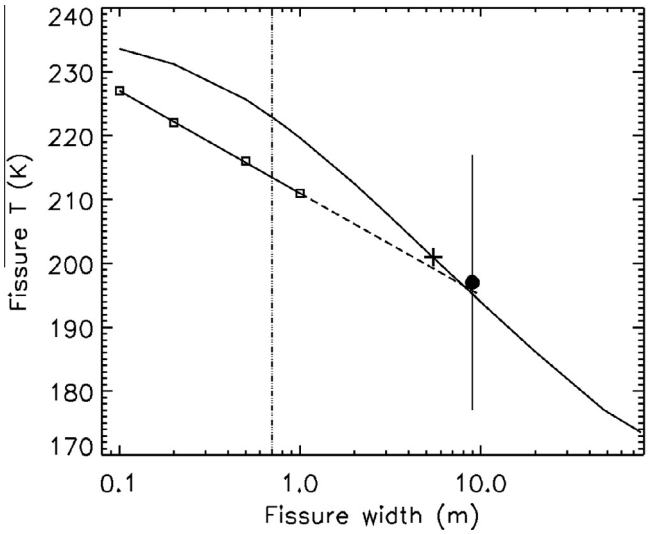

Fig. 4. Fissure models: the solid, upper curve is the combinations of fissure width and temperature that best match the measured VIMS radiance spectrum for models that include the contribution of radiance from the fissure plus the conductively heated margins. The end member of this suite of models is the 'zero-width' fissure with T = 236.5 K (Table 2, case f – not shown here; fit is shown in Fig. 3). The vertical dash-dotted line indicates where the contribution to the VIMS radiance from the fissure is equal to that from the margins, 0.7 m width, T = 222.9 K. For fissures wider than 0.7 m, the VIMS spectrum is dominated by radiance from the fissure; for fissures narrower than 0.7 m, the VIMS spectrum is dominated by the radiance from the margins. The solid circle with error bars is the T_{color} isothermal model. The + symbol is the best fit fissure plus margins model (Table 2, case d) when both the width and temperature are allowed to vary. The square symbols are hydrodynamic models of viscous water vapor flow through an ice walled fissure with heat exchange between the vapor and walls from Ingersoll and Pankine (2010), their Table 1. The square symbols are their models 1–4 with vertical walls and different widths. The solid straight line shows the trend through these 4 models and the dashed line the extrapolation of this trend to larger fissure widths.

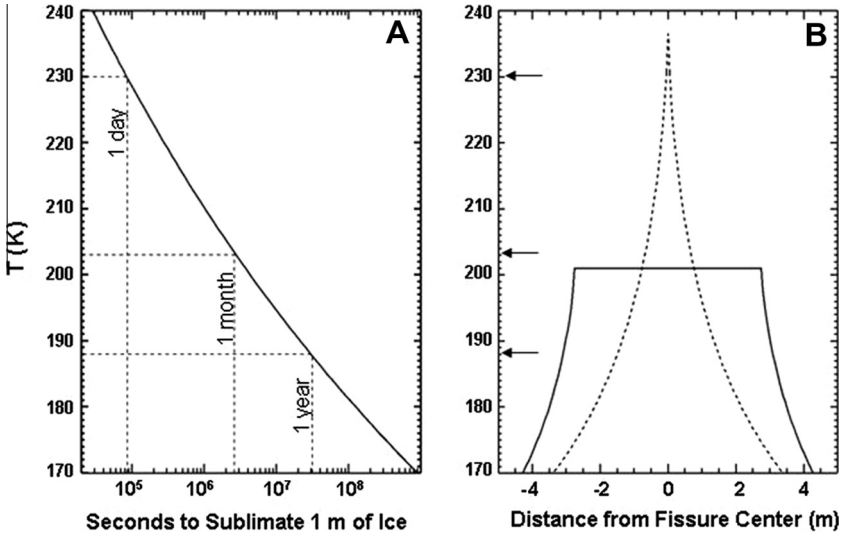

Fig. 5. (A) The time to sublimate a 1 m thick layer of pure ice 1 h over the range of temperatures relevant to Enceladus fissures. The horizontal ice surface of the margins adjacent to the fissure wall will erode 1 m/day if the ice is held at 230 K; 1 m/month if the ice is held at 203 K; and 1 m/year if the ice is held at 188 K. (B) T profiles for two different fissure models that match the VIMS spectrum. The dashed line is the margins-dominated, zero width end member with T = 236.5 K (Table 2, case f). The solid line is best fit conduction-included model with T = 200.9 K and w = 5.5 m (Table 2, case d). From top to bottom, the three arrows show the temperatures corresponding to the 1 m/day, 1 m/month and 1 m/year sublimation rates, respectively.

dashed line in Fig. 3. This margins-dominated zero-width end member fits the spectrum nearly as well as the fissure-dominated nominal best fit and cannot be excluded from consideration based on the VIMS spectrum alone.

The question that needs to be resolved is: Does the VIMS spectrum detect the radiance from the fissure or from the margins? The boundary between these two regimes occurs where the contributions to the VIMS radiance from the fissure and margins are equal. For the family of fissure-plus-margins models in Fig. 4, this boundary occurs at a w = 0.7 m and T = 222.9 K. For narrower fissures, the VIMS spectrum is 'margins-dominated' and for wider fissures the VIMS spectrum is 'fissure-dominated'.

To address which case applies to the Enceladus fissures, consider the temperature dependence of the vapor pressure of ice, $e(T)$. Ingersoll and Pankine (2010) give an approximation to the vapor pressure of ice that is accurate to <3% for 160 K < T < 273 K, $e(T) = A \exp(-B/T)$ where $A = 3.63 \times 10^{12}$ Pa and B = 6147 K. Fig. 5(a) shows the time needed to sublimate 1-m thickness of ice, $\tau = \rho(2\pi RT)^{1/2}/e(T)$, where ρ is the 926 kg m^{-3} density of ice at 200 K and R = 462 J (kg K)$^{-1}$, the ideal gas constant per molar mass of H_2O. A meter-thick layer of pure ice held at 230 K will sublimate completely away in 1 day. In Fig. 5(b) these meter-sublimation timescales are compared to profiles of T with distance from the fissure center for the zero-width margins-dominated model and the nominal best fit T = 200.9 K, w = 5.5 m fissure-dominated model, both of which match the VIMS spectrum. Narrow margins-dominated fissures with T > 220 K will sublimate a meter of ice from the warm margin surface immediately adjacent to each fissure wall within a few days. This rapid erosion will deepen and widen the fissure opening to meter-scales.

Ingersoll and Pankine (2010) model hydrodynamic flow of H_2O vapor between ice walls for a range fissure geometries to investigate under what conditions the ice melts at depth. They find that "the partial pressure of the vapor ... is nearly equal to the saturation vapor pressure of the ice" and that this quasi-equilibrium state is quickly achieved over most of the fissure depth. Their models predict the temperature at the top of the fissure for a range of fissure widths and vertical profiles (Fig. 4). Their models 1–4 are similar parallel vertical wall fissures with only the width changing from 0.1 to 1 m, defining the trend of variation of T with w shown by the straight line in Fig. 4. Their w < 1 m models are too cool by ~10 K to supply sufficient radiance to match the VIMS spectrum. However, if their trend is extrapolated to larger widths as indicated by the dashed line in Fig. 4, it intersects the curve of the combinations of w and T that match the VIMS spectrum very close to the isothermal T_{color} model and the best fit conduction-included model locations. This suggests that wider and cooler fissures consistent with the physics in the Ingersoll and Pankine (2010) models can also match our VIMS spectrum. It is noteworthy that their model 6 (Ingersoll and Pankine, 2010) with a fissure that widens from 0.1 m at 50 m depth to 1 m at the surface has the same T at the top, 211 K, as model 1 which has constant 1 m width. This suggests that the T at the top of the fissure is only weakly dependent on changes in the fissure geometry not far below the surface. Model 6 (Ingersoll and Pankine, 2010) is also consistent with melting at depth.

Consider a hypothetical initial surface eruption of T > 220 K water vapor from depth initiating a narrow w < 0.1 m crack in Enceladus surface ice. The ice immediately adjacent to the crack is heated by conduction to a similar high temperature where sublimation erodes the surface layer to meter depth within a few days. This widening of the fissure opening results in lowering of T of the vapor at the fissure opening, as in the Ingersoll and Pankine (2010) models, decreasing the rate of sublimation. When the vapor T is reduced to 203 K, the meter erosion time increases to a month. In addition, as the vapor T decreases, less distance from the fissure wall of the adjacent margin surface is heated to rapid sublimation and the process slows. Fissures that are stable for months can be expected to have surface expressions that correspond to widths of several meters and $T \sim 203$ K. Although active fissures will continue to widen and cool, this process will slow significantly due to the strong T dependence of the ice vapor pressure. From this perspective, the T and w deduced from our measured VIMS spectrum are consistent with this quasi-equilibrium state of an active water vapor eruption into space from an ice fissure that has been active for months or longer. Although the durations of individual fissure eruptions are not precisely constrained by Cassini observations, the plumes of vapor and particles erupting from the fissures have persisted for many months during the mission (Porco et al., 2006; Ingersoll and Ewald, 2011; Spencer et al., 2009; Hedman et al., 2009; Spitale and Porco, 2007).

This hypothesis of widening and deepening of ice crack openings due to warm vapor flowing through them should apply to other icy surfaces on airless bodies. For example, on Jupiter's satellite Europa, linear fissures are abundant in an ice-rich crust covering a liquid water ocean layer. If water vapor escapes through fissures in cold ice, our hypothesis predicts that the surface thermal expression at active fissures is likely to be detected as ~200 K emission over widths of several meters.

4.2. Mass and power loss rates from fissure models that match the VIMS spectra

The VIMS measurements reported here are an extraordinary high spatial resolution slice across *one* of the Enceladus South Pole fissures at *one* location. To place these VIMS results within the context of published observations that characterize the entire South Pole fissure activity, we calculate the mass and power loss rates per unit length of fissure for fissure models that match our VIMS spectrum. Two important observational constraints on the 'big picture' of the entire South Pole fissure activity are the total water vapor mass loss rate estimated from UVIS measurements of occultations of stars and the Sun by the plumes (Hansen et al., 2006, 2008, 2011) and the total power radiated from the South Pole region estimated from CIRS spectra covering large areas of the South Pole using a broad range of wavelengths greater than 7 μm (Spencer et al., 2006, 2013). We emphasize that the VIMS data reveal new details of the warmest component of the fissure emission at one location. We put our VIMS results in context by comparing the mass and power loss rates per unit length of fissure for models that match the VIMS results at Baghdad Sulcus to the average mass loss rate per unit length of fissure deduced from the UVIS occultation data and the average radiated power per unit length of fissure estimated from CIRS spectra. These averages assume a total fissure length of 500 km consistent with Ingersoll and Pankine (2010).

In Table 2(A), we estimate Q_{rad}, the power radiated to space per meter of fissure length, Q_{vap}, the power carried away as latent heat of the vapor per meter of fissure length, dM/dt, the mass loss rate of H_2O vapor for each kilometer of fissure length, and $Q_{total} = Q_{rad} + Q_{vap}$ for the three isothermal model cases plotted in Fig. 3. Explicitly, $Q_{rad} = w\sigma(T^4 - T_b^4)$, where T is the fissure temperature, w the fissure width, T_b the background temperature of 75 K (Abramov and Spencer, 2009), and σ is the Stefan–Boltzmann constant. Following Ingersoll and Pankine (2010) the mass loss rate per unit length of the fissure is $dM/dt = we(T)\,(2\pi RT)^{-1/2}$. Finally, $Q_{vap} = L\,dM/dt$, where $L = 2.8 \times 10^6$ J kg^{-1}, the latent heat of vaporization for H_2O ice.

4.2.1. Mass loss rates

The total mass loss rate of H_2O vapor supplying the plumes determined from the UVIS occultation results is $dM/dt = 200 \pm 30$ kg s^{-1} assuming $T = 170$ K (Hansen et al., 2011). For other temperatures, this dM/dt estimate is proportional to the thermal velocity of the molecules and scales as $T^{1/2}$. For $T = 197$ K, the T-corrected UVIS $dM/dt = 215 \pm 32$ kg s^{-1} which corresponds to 0.43 ± 0.06 kg s^{-1} km^{-1} for the average mass loss rate along 500 km of total fissure length.

For the nominal isothermal T_{color} fissure (case a), each km of fissure length supplies 1.21 kg s^{-1} of H_2O vapor to the plume. This mass loss rate per km of fissure length for case a is nearly three times the average needed to supply the UVIS mass loss constraint. This suggests that the VIMS measurement sampled an active portion of the fissure that was supplying mass to the plume at a much greater than average rate. The cooler and wider fissure model (case b) supplies only 10% of mass supplied by the case a model and only 30% of the average UVIS mass loss rate.

Table 2(B) gives the power and mass loss rates for the non-isothermal fissure plus conductively heated margins models for the best fit (case d) and lower T (case e) and upper T (case f) limits. Case d is similar to case a. The fissure contribution to dM/dt can easily supply the UVIS average mass loss rate and the cooler margins contribute little additional mass loss. Case e, like case b, is too cool to supply the average UVIS mass loss rate with the additional margins contributing little. In Section 4.1.2.2 we have shown that the high T models in cases c and f would be short-lived and will rapidly evolve towards cases a and d.

We conclude that the mass loss rate is dominated by the warm fissure component and that $T \sim 200$ K is sufficient to supply the UVIS occultation mass loss rate constraint from a fraction of the total length of fissures at Enceladus South Pole.

4.2.2. Radiated power

Estimates of the total endogenic power radiated from Enceladus' South Pole region vary due to the inherent difficulty of measuring the endogenic power contributed by areas that are heated only slightly above the background temperature. CIRS FP3 spectra were used to estimate the radiated power as $H = 5.8 \pm 1.9$ GW (Spencer et al., 2006). CIRS FP1 spectra, which are sensitive to longer wavelengths and lower temperatures, were used to estimate the total radiated power as $H = 15.8 \pm 3.1$ GW (Howett et al., 2011). A new analysis (Spencer et al., 2013) of high spatial resolution CIRS data allows the fissure emission to be spatially separated from the background and modeled as a combination of high and low temperature components. The low temperature component is

Table 2
A comparison of Enceladus fissure models.

Case	Fissure contribution					Margins contribution			Fissure + Margins		
	T (K)	w (m)	Q_{rad} (kW m^{-1})	Q_{vap} (kW m^{-1})	dM/dt (kg s^{-1} km^{-1})	Q_{rad} (kW m^{-1})	Q_{vap} (kW m^{-1})	dM/dt (kg s^{-1} km^{-1})	Q_{rad} (kW m^{-1})	Q_{total} (kW m^{-1})	Notes
(A) Isothermal models: fissure only											
a	197	9	0.75	3.40	1.21	0	0	0	0.75	4.15	T_{color}
b	172	77[a]	3.68	0.33	0.12	0	0	0	3.68	4.01	Filled, $f = 1$
c	273[a]	0.1	0.03	190	67.9	0	0	0	0.03	190	T_{melt}
(B) Non-isothermal Models: Fissure + conductively heated margins											
d	200.9	5.5	0.50	3.77	1.35	3.65	0.10	0.04	4.15	8.02	Best fit
e	173.5	77[a]	3.82	0.45	0.16	2.85	0.02	0.001	6.67	7.14	Filled, $f = 1$
f	236.5	0[a]	0	0	0	4.64	4.12	1.47	4.64	8.76	Zero-width (Abramov and Spencer, 2009)

Column definitions: (1) Model case identifier; (2) T, fissure temperature; (3) w, fissure width; (4) Q_{rad}, power radiated per unit length of fissure; (5) Q_{vap}, power carried away as latent heat of the H_2O vapor from the fissure; (6) dM/dt, H_2O vapor mass loss rate from the fissure; (7, 8 and 9) are the same physical quantities as 4, 5 and 6, but for the contribution from the conductively heated *margins* within 1 km of the fissure; (10) total radiated power; (11) total power lost (sum of columns 4, 5, 7 and 8 from each meter length of active fissure plus margins. All quantities are the contributions above a background level defined by replacing the fissure and margins with 75 K background ice surface. For comparison with the models, observational constraints are $dM/dt = 0.43$ kg s^{-1} km^{-1} and $Q_{rad} = 5.4$ kW m^{-1} (see text).

[a] Parameter value held constant during least squares fit to spectrum from Fig. 3.

needed to match the long wavelength FP1 data, but makes a negligible contribution to the radiance at the short wavelengths of our VIMS measurements. For our purpose of comparison with VIMS spectra and models in Table 2, the most appropriate estimate of the observational constraint on the average radiated power per unit length of fissure is that from the high temperature component (Spencer et al., 2013), $\langle Q_{rad} \rangle$ = 2.7 GW/500 km = 5.4 kW m^{-1}.

From Table 2, it is clear that Q_{rad} in the models is dominated by the contributions from larger and cooler area model components. For case a, the fissure contributes only 14% of the average 5.4 kW m^{-1}. Although case b contributes 68% of $\langle Q_{rad} \rangle$, case b cannot supply the mass loss rate. Case d can nearly satisfy both the mass and radiation constraints. The high temperature of the fissure component contributes a high mass loss rate while the warm area of the convectively heated margins supplies 77% of $\langle Q_{rad} \rangle$. Note that for case d, the rate of power lost to escaping vapor Q_{vap} from the fissure is nearly equal to the rate of power lost to radiation from the margins. Case e, like case b, increases Q_{rad} at the expense of decreasing dM/dt.

Conduction of heat from the warm fissure walls through the adjacent ice and cooling by radiation to space (Abramov and Spencer, 2009) must occur and needs to be included in any physical model of the fissures. Additional processes are also likely to influence the temperature distribution around the fissures. Sublimation cooling, heat carried back to the surface and redistributed by warm ice particles and condensation of vapor, plus the possibility of extended sub-surface heat sources all need further modeling.

5. Conclusions

We have shown that fissures < 1 m wide and with T > 220 K will rapidly widen at their mouths within days due to sublimation erosion caused by the exponential increase of the vapor pressure of ice with increasing T. Fissure models > 1 m wide that match the VIMS spectrum all have more radiance contributed by the fissure in the VIMS spectral range than by the margins. Applying the Abramov and Spencer (2009) model to our 197 K fissure, we calculate that the 3–5 μm wavelength-integrated radiance from the conductively heated surface next to the fissure, but still within the area sampled during the detection integration, contributes only 11% of the wavelength-integrated radiance from the fissure itself. A similar result (17%) is obtained for the best fit of a more complicated 'conduction-included' model. We conclude that the radiance at VIMS wavelengths is dominated by emission from the warmest temperature ice visible within the fissure width.

The VIMS line of sight to the fissure was only 13° from the vertical at the time of the measurement providing a direct view into the fissure to a depth of $\leqslant$4.4 times the fissure width for a 9 m wide fissure with vertical walls, about 40 m. The solid angle subtended by the fissure as seen by VIMS would be filled by the upper walls of the fissure. We interpret the 197 K temperature as a measurement of the average temperature of the upper few tens of meters of the vapor-heated ice walls inside the fissure.

The process of widening of the fissure mouth due to rapid sublimation of the adjacent ice surface should apply to other cold icy satellites, e.g. Europa, and to the other tiger stripe fissures on Enceladus. Wherever H_2O vapor at temperatures significantly exceeding 200 K escapes through a narrow fissure in the surface for a few months duration, the mouth widens, the escaping gas cools and erosion slows. A metastable active fissure should exhibit a thermal spectrum representative of a 200 K isothermal source several meters wide, as we observe at Baghdad Sulcus. Future missions seeking to identify persistent active H_2O vapor eruption sites on icy airless satellites might apply this model to optimize the sensitivity of their instruments to active fissures.

Our VIMS high-spatial-resolution measurements of a single location along Baghdad Sulcus are not well-suited for extrapolation to characterization of the Enceladus South Pole activity at the large scale. Yet these measurements do provide new observational constraints on the width and the temperature at the top of the fissures that can be viewed in the context of published models and other measurements. Key independent observational constraints on the total H_2O-vapor mass-loss rate supplying the plumes (Hansen et al., 2011) and the radiated power loss from the endogenically heated fissures (Spencer et al., 2013) are compatible with our models that combine a finite width fissure with conductively heated margins. Temperatures near 200 K within the fissure width are needed to supply the observed mass loss rate while an extended area of conductively heated margin adjacent to the fissure is needed to contribute the observed radiated power. Models that correspond to the widest and coolest fissures compatible with the VIMS spectrum are not compatible with the observed mass loss rate.

The mass escape rate per km of fissure (model cases a and d) is ~3 times the estimated average for the fissures which suggests that the VIMS detection is sampling an active plume source area and that 178 km of fissure length active at this rate could supply the total mass of the plumes. The observation that there are distinct plumes emanating from multiple discrete source regions along the fissures (Spitale and Porco, 2007) is consistent with this picture. The key 'record number 33' occultation point of maximum optical depth (Hansen et al., 2008, 2011; Tian et al., 2007), used to calibrate the plume models, passes very near the location of our VIMS source (Table 1) and the plume 1 source in Spitale and Porco (2007). The most probable speed for H_2O molecules at 197 K is 426 m s^{-1}, consistent with the Tian et al. (2007) ballistic plume models which suggest that water molecules feeding the plumes leave the near surface at velocities from 300 to 500 m s^{-1}.

The total heat flow from Enceladus' South Pole region is dominated by emission from large areas at much lower T than the fissure measured here (Spencer et al., 2006; Abramov and Spencer, 2009). Measurements at much longer wavelengths are required to address the total power balance (Howett et al., 2011; Spencer et al., 2013).

At the time of our VIMS observation, Enceladus was near the apocenter of its eccentric orbit (true anomaly = 193°, orbital phase = 0.54), where models predict that the fissures should be under the strongest tensional stresses (Hurford et al., 2007, 2009; Smith-Konter and Pappalardo, 2008).

The combination of rapid sampling of spectra, a low-altitude flyby over the South Pole during the winter night, expert planning by the Cassini mission personnel, and luck allowed us to measure the width and temperature of the walls at the top of an active fissure on Enceladus, very likely while it was supplying vapor to a plume.

Acknowledgments

We acknowledge the Cassini Navigation Team and coordination with the INMS and CIRS teams that enabled these observations. We are grateful to the two anonymous referees for their insightful comments that improved the final manuscript. This work was supported in part by the Cassini Project at the Jet Propulsion Laboratory, California Institute of Technology under a contract with the National Aeronautics and Space Administration and in part by a grant from the NASA Outer Planets Research Program.

Appendix A. Interpretation of the fill factor for a linear fissure moving through a pixel

For most thermal emission radiance measurements where the instrument points steadily at a stationary target, the 'fill factor' is simply the fraction of the area of the planet's surface within the field of view that is warm enough to radiate at the wavelength of interest. But for our VIMS measurements of Enceladus, the interpretation is more complicated because the narrow emitting fissure is moving

rapidly and crosses the entire solid angle that the pixel sees in a fraction of the 0.025 s integration time as a consequence of low 74 km altitude and high 7.5 km s^{-1} velocity of the Cassini spacecraft. In this appendix, we define the fill factor for this moving target case and determine the accuracy of a simple approximation for the relevant geometry.

Fig. A1 illustrates the geometry of a linear fissure sweeping past the VIMS pixel and the change in area (∼signal) detected during one 0.025 s integration time sample.

We define the 'fill factor' f as the ratio of the measured signal to the signal that would be measured if the same temperature source completely filled the pixel during the entire integration. For an isothermal fissure:

$$f = S_w/S = \int BA_w(t)dt/BA\tau = \int A_w(t)\,dt/A\tau \qquad \text{(A1)}$$

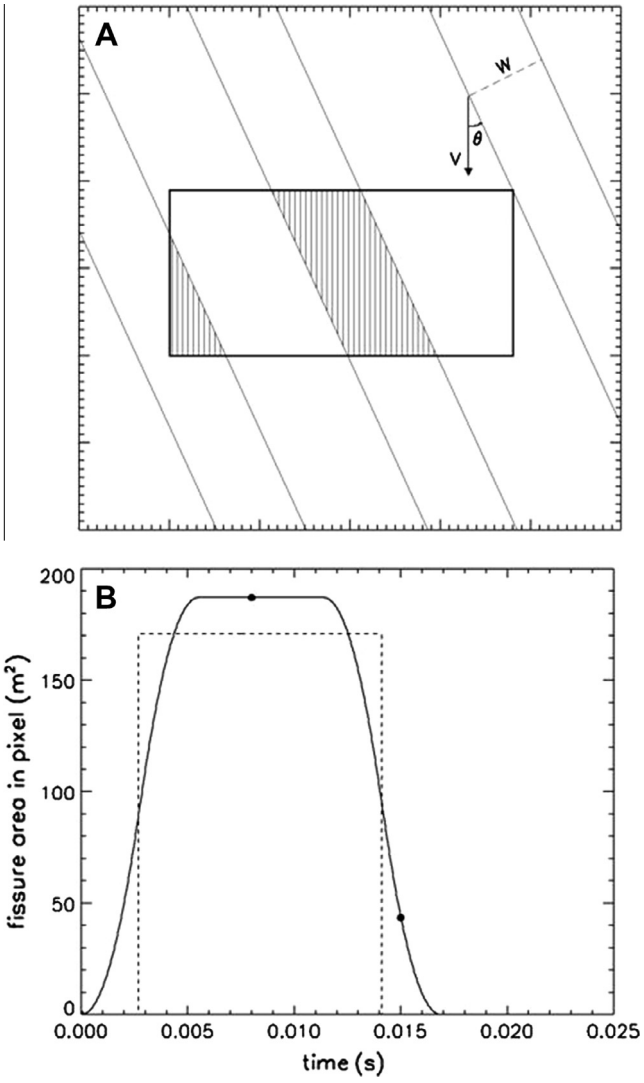

Fig. A1. (A) View from the detector drawn to scale for the Enceladus observation geometry with each small tick mark = 1 m. The solid rectangle at center is the 38 m × 19 m VIMS high-resolution pixel field of view projected on Enceladus surface as the spacecraft moves in the +y direction with velocity v = 7.5 km s^{-1} over a linear fissure of width w = 9 m oriented at an angle θ = 24° relative to v. Seen from the detector, the fissure appears to sweep through the pixel from right to left. The fissure is shown at three times: (1) at 1st contact with the pixel, (2) near the pixel center, and (3) leaving the pixel. The shaded area is the area of the fissure that is within the pixel field of view. (B) The area of the fissure that is in the pixel field of view as a function of time during one 0.025 s integration. Solid line is the exact calculation and dots are the shaded areas at times 2 and 3. The dashed line is the 'square wave' approximation for a vertical rectangle with area w × 19 m that crosses the pixel width in 38 m/(v tan θ).

where S_w is the measured signal from the fissure, S is signal from a completely filled pixel, B is the Planck radiance function, $A_w(t)$ is the area of the fissure in the pixel at time t as illustrated in Fig. A1, A is area of the pixel illustrated by the rectangle in Fig. A1(a), and τ is the duration of the integration. The integral on the right hand side of Eq. (A1) is just the area under the solid curve in Fig. A1(b). For a stationary fissure, A_w is constant and f simplifies to A_w/A, the more familiar case.

The 'square wave' approximation (dashed line in Fig. A1(b)) which can be visualized as just a vertical rectangle of width w and pixel height moving to the left in Fig. A1 a with the velocity v tan θ. This approximation leads to a simple relationship between f and w: $f = w/(v\tau \tan\theta)$ which was used in Section 4.1. For the geometry of our Enceladus fissure spectrum, the exact calculation matches the best fit f = 0.12 for a fissure width of 9 m. The square wave approximation for f = 0.12 corresponds to w = 10 m. This difference is small compared to the other errors and throughout the text, we cite the exact calculation w = 9 m without going into a lengthy discussion of the insignificant difference between the exact and easier to convey square wave approximation.

References

Abramov, O., Spencer, J.R., 2009. Endogenic heat from Enceladus' south polar fractures: New observations, and models of conductive surface heating. Icarus 199, 189–196.

Acton, C.H., 1996. Ancillary data services of NASA's Navigation and Ancillary Information Facility. Planet. Space Sci. 44, 65–70, <http://naif.jpl.nasa.gov/naif/toolkit.html>.

Anderson, J.A. et al., 2004. Modernization of the integrated software for imagers and spectrometers. Lunar Planet. Sci. XXXV. Abstract 2039.

Archinal, B.A. et al., 2010. Report of the IAU Working Group on Cartographic Coordinates and Rotational Elements of the Planets and Satellites: 2009, Cassini ECR-100654.

Brown, R.H. et al., 2004. The Cassini Visual and Infrared Mapping Spectrometer (VIMS) investigations. Space Sci. Rev. 115, 111–168.

Dougherty, M.K. et al., 2006. Identification of a dynamic atmosphere at Enceladus with the Cassini magnetometer. Science 311, 1406–1409.

Hansen, C.J. et al., 2006. Enceladus' water vapor plume. Science 311, 1422–1425.

Hansen, C.J. et al., 2008. Water vapor jets inside the plume of gas leaving Enceladus. Nature 456, 477–479.

Hansen, C.J. et al., 2011. The composition and structure of the Enceladus plume. Geophys. Res. Lett. 38, L11202. http://dx.doi.org/10.1029/2011GL047415.

Hedman, M.M. et al., 2009. Spectral observations of the Enceladus plume with Cassini–VIMS. Astrophys. J. 693, 1749–1762.

Howett, C.J.A., Spencer, J.R., Pearl, J., Segura, M., 2011. High heat flow from Enceladus' south polar region measured using 10–600 cm^{-1} Cassini/CIRS data. J. Geophys. Res. 116, E03003. http://dx.doi.org/10.1029/2010JE003718.

Hurford, T.A., Helfenstein, P., Hoppa, G.V., Greenberg, R., Bills, B.G., 2007. Eruptions arising from tidally controlled periodic openings of rifts on Enceladus. Nature 447, 292–294.

Hurford, T.A. et al., 2009. Geological implications of a physical libration on Enceladus. Icarus 203, 541–552.

Ingersoll, A.P., Ewald, S.P., 2011. Total particulate mass in Enceladus plumes and mass of Saturn's E ring inferred from Cassini ISS images. Icarus 216, 492–506.

Ingersoll, A.P., Pankine, A.A., 2010. Subsurface heat transfer on Enceladus: Conditions under which melting occurs. Icarus 206, 594–607.

Kieffer, S.W. et al., 2006. A clathrate reservoir hypothesis for Enceladus' south polar plume. Science 314, 1764–1766.

Kieffer, S.W., Lu, X., McFarquar, G., Wohletz, K.H., 2009. A redetermination of the ice/vapor ratio of Enceladus' plumes: Implications for sublimation and the lack of a liquid water reservoir. Icarus 203, 238–241.

Matson, D.L., Castillo-Rogez, J.C., Davies, A.G., Johnson, T.V., 2012. Enceladus: A hypothesis for bringing both heat and chemicals to the surface. Icarus 221, 53–62.

Porco, C.C. et al., 2006. Cassini observes the active South Pole of Enceladus. Science 311, 1393–1401.

Postberg, F. et al., 2009. Sodium salts in E ring ice grains from an ocean below the surface of Enceladus. Nature 459, 1098–1101.

Postberg, F., Schmidt, J., Hillier, J., Kempf, S., Srama, R., 2011. A salt-water reservoir as the source of a compositionally stratified plume on Enceladus. Nature 474, 620–622, doi:10.1038/nature10175.

Roatsch, T. et al., 2008. High-resolution Enceladus atlas derived from Cassini ISS images. Planet. Space Sci. 56, 109–116.

Schmidt, J., Brilliantov, N., Spahn, F., Kempf, S., 2008. Slow dust in Enceladus plume from condensation and wall collisions in tiger stripe features. Nature 451, 685–688.

Smith-Konter, B., Pappalardo, R.T., 2008. Tidally driven stress accumulation and shear failure of Enceladus's tiger stripes. Icarus 198, 435–451.

Spencer, J.R. et al., 2006. Cassini encounters Enceladus: Background and the discovery of a south polar hot spot. Science 311, 1401–1405.
Spencer, J. et al., 2009. Enceladus: An active cryovolcanic satellite. In: Dougherty, M.K. et al. (Eds.), Saturn from Cassini–Huygens. Springer, pp. 683–724.
Spencer, J.R. et al., 2010. Observations of thermal emission from the South Pole of Enceladus in August 2010. Paper presented at the EPSC-DPS Joint Meeting held at Nantes, France, October 2011, p. 1630. <http://meetings.copernicus.org/epsc-dps2011>.
Spencer, J.R. et al., 2012. The spatial distribution of thermal emission from Baghdad Sulcus, Enceladus at 100 m scales. Paper #104.06 presented at the 44th Annual Meeting of the Division of Planetary Sciences of the American Astronomical Society, Reno, NV, October 2012.
Spencer, J.R. et al., 2013. Enceladus heat flow from high spatial resolution thermal emission observations, EPSC Abstracts, vol. 8, EPSC2013-840-1.
Spitale, J.N., Porco, C.C., 2007. Association of the jets of Enceladus with the warmest regions on its south-polar fractures. Nature 449, 695–697.
Thomas, P.C. et al., 2007. Shapes of the saturnian icy satellites and their significance. Icarus 190, 573–584.
Tian, F., Stewart, A.E.F., Toon, O.B., Larsen, K.W., Esposito, L.W., 2007. Monte Carlo simulations of the water vapor plumes on Enceladus. Icarus 188, 154–161.